ER membranes exhibit phase behavior at sites of organelle contact

Christopher King[a], Prabuddha Sengupta[a], Arnold Y. Seo[a], and Jennifer Lippincott-Schwartz[a,1]

[a]Janelia Research Campus, Howard Hughes Medical Institute, Ashburn, VA 20175

Contributed by Jennifer Lippincott-Schwartz, February 6, 2020 (sent for review June 25, 2019; reviewed by Barbara Baird and Tobias Baumgart)

The endoplasmic reticulum (ER) is the site of synthesis of secretory and membrane proteins and contacts every organelle of the cell, exchanging lipids and metabolites in a highly regulated manner. How the ER spatially segregates its numerous and diverse functions, including positioning nanoscopic contact sites with other organelles, is unclear. We demonstrate that hypotonic swelling of cells converts the ER and other membrane-bound organelles into micrometer-scale large intracellular vesicles (LICVs) that retain luminal protein content and maintain contact sites with each other through localized organelle tethers. Upon cooling, ER-derived LICVs phase-partition into microscopic domains having different lipid-ordering characteristics, which is reversible upon warming. Ordered ER lipid domains mark contact sites with ER and mitochondria, lipid droplets, endosomes, or plasma membrane, whereas disordered ER lipid domains mark contact sites with lysosomes or peroxisomes. Tethering proteins concentrate at ER–organelle contact sites, allowing time-dependent behavior of lipids and proteins to be studied at these sites. These findings demonstrate that LICVs provide a useful model system for studying the phase behavior and interactive properties of organelles in intact cells.

endoplasmic reticulum | contact sites | phase partitioning | organelle tethers

It has long been hypothesized that small, diffraction-limited, liquid-ordered (L_o) microdomains can form on the plasma membrane (PM) of cells (1–3). Lipids such as cholesterol and sphingolipids are concentrated in these domains, and membrane and membrane-associated proteins can preferentially segregate into these domains to allow sorting of proteins and localized signal transduction (2, 4). Giant PM vesicles (GPMVs) isolated from mammalian PM have been an important tool for studying these properties in physiological membranes (5–8). GPMVs contain the complex mixture of lipids and proteins found in intact PM, are not contaminated with membranes from other organelles, and phase-separate into microscopically visible L_o-like and liquid-disordered-like lipid domains (8). These features make GPMVs a suitable model system for studying the lipid domain preference of membrane proteins (7, 9, 10). Phase-like membrane heterogeneities with physical properties similar to the lipid phases in GPMVs are also thought to occur in the intact PM, albeit on a smaller scale due to constant lipid turnover and membrane trafficking (11). As an example, a recent study demonstrated a functional role of lipid-based phase separation in mammalian PM by showing ordered L_o-like domain formation during HIV assembly at the PM, a process driving sorting of specific proteins into HIV membranes (4).

A drawback of GPMVs is that they can only be used for studying biophysical properties of proteins and lipids that localize to the PM (12). However, many fundamental processes of protein sorting and signal transduction occur on surfaces of intracellular organelles. Various organelles, including endoplasmic reticulum (ER), lysosomes, endosomes, peroxisomes, mitochondria, and lipid droplets (LDs), have distinct membrane compositions and communicate with each other through either membrane trafficking pathways or membrane contact sites (13–17). The membrane contact sites represent only a small proportion of the overall surface area of an organelle, but they serve several fundamental functions, including being the sites of interorganelle exchange of lipids, ions, reactive oxygen species, and other small molecules (18–22). Contact sites also play an important role in organelle inheritance and maintenance (18, 21–29). Even though known tethering, effector, and regulatory proteins involved in contact site organization have been uncovered, it is unclear how contact sites assemble and whether they exhibit self-organizational properties of lipids and proteins (18). This ambiguity is largely due to the difficulty of studying the time-dependent behavior of lipids and proteins at nanoscopic contact sites (8, 11).

The ER is the largest organelle within the cell and is responsible for many cellular processes, including the synthesis of proteins and lipids (30). The ER also contacts all other organelles (17). Here, we demonstrate that hypotonic swelling of adherent cells forms ER-derived, Large Intracellular Vesicles (ER LICVs) that can be used as a tool for investigating the self-organizing and phase behavior of ER membranes. ER LICVs do not rupture in cells and they can be rapidly retubulated to form a complex ER network. When cells are cooled below room temperature, ER LICVs display reversible, microscopically observable phase domains of ER-ordered (ER_o) and ER-disordered (ER_d) membrane content. Hypotonic swelling generates stable LICVs from other membrane-bound organelles, which contact ER LICVs in phase-separated domains with concentrated interorganellar tethering proteins. LICVs generated with hypotonic swelling thus represent a model system that can be used to study the biochemical and biophysical properties of intracellular organellar membranes in intact eukaryotic cells.

Significance

Membrane phase behavior in cells permits transient concentration of specific proteins and lipids into dynamic nanoscopic domains. Here, we tested the existence and role of such phase behavior in endoplasmic reticulum (ER) membranes. Employing hypotonic cell swelling, we created large intracellular vesicles (LICVs) from internal organelles. ER LICVs maintained stable interorganelle contacts, with known protein tethers concentrated at the contact sites. Cooled ER LICVs underwent reversible phase separation into microscopically visible domains with different lipid order and membrane fluidity. The phase-separated domains specified sites of contact between the ER and different organelles.

Author contributions: C.K., P.S., A.Y.S., and J.L.-S. designed research; C.K. performed research; C.K. analyzed data; and C.K., P.S., A.Y.S., and J.L.-S. wrote the paper.

Reviewers: B.B., Cornell University; and T.B., University of Pennsylvania.

The authors declare no competing interest.

See online for related content such as Commentaries.

[1]To whom correspondence may be addressed. Email: lippincottschwartzj@janelia.hhmi.org.

This article contains supporting information online at https://www.pnas.org/lookup/suppl/doi:10.1073/pnas.1910854117/-/DCSupplemental.

First published March 16, 2020.

CELL BIOLOGY

Results

Hypotonic Treatment Vesiculates the ER in Adherent Cells. COS7 cells were transiently transfected to coexpress Sec61β-mNeonGreen (Sec61β-mNG) to identify ER membranes and KDEL-mCherry to label the ER lumen (31, 32). Before cell swelling by hypotonic treatment, the ER existed as a fine tubular network extending throughout the cytoplasm and surrounding the nuclear envelope (Fig. 1*A*, Isotonic). In these cells, the ER membrane and lumen markers had overlapping distributions due the diffraction-limited width of ER tubules. After incubation at 37 °C for 10 min in hypotonic swelling media, however, the ER's fine tubular network transformed into numerous micrometer-sized LICVs composed of Sec61β-positive membranes filled with KDEL-mCherry (Fig. 1*A*, Hypotonic). No dispersal of KDEL-mCherry into the cytoplasm was observed, indicating that the integrity of ER membrane was maintained during hypotonic treatment. Many cells exhibited complete and dramatic transformation of the tubular ER network into micrometer-scale LICVs (Fig. 1*A*, Hypotonic), although cell-to-cell heterogeneity in the degree and size of ER LICV generation was observed. We quantified the propensity for ER LICV generation in several cell types including HEK293T, U2OS, and COS7. Larger, flatter cells like COS7 and U2OS cells showed a higher proclivity for ER LICV production, with ∼30 to 40% of cells containing ER LICVs (Fig. 1*B*).

Sec61β-mNG fluorescence associated with a single ER LICV structure did not recover after photobleaching (Fig. 1*C*), indicating that there is no exchange of membrane proteins between separate ER LICV structures in cells. Also, photobleaching of KDEL-mCherry within the lumen of a single ER LICV showed no fluorescence recovery from neighboring ER LICVs, indicating that ER LICVs are not connected via continuous membrane linkages (Fig. 1*D*).

Given the dramatic change in ER morphology from a tubular network in isotonic media to ER LICVs under hypotonic conditions, we examined the ER's ability to regenerate a tubular morphology from LICVs. Following replacement of hypotonic media with isotonic media, ER LICVs rapidly tubulated and reconnected to form a reticular network of ER tubules within 2 min (Fig. 1*E* and Movie S1). The reversibility of the process suggests that successive treatment of cells with hypotonic and isotonic media can be used to investigate the mechanisms of various ER membrane remodeling phenomena such as tubulation and fusion (33–35).

ER LICVs Exhibit Reversible, Temperature-Dependent Phase Separation. The membrane of the ER is thinner than the PM due to its reduced cholesterol content and it has yet to be shown that this membrane has the physical–chemical capacity for temperature-dependent phase

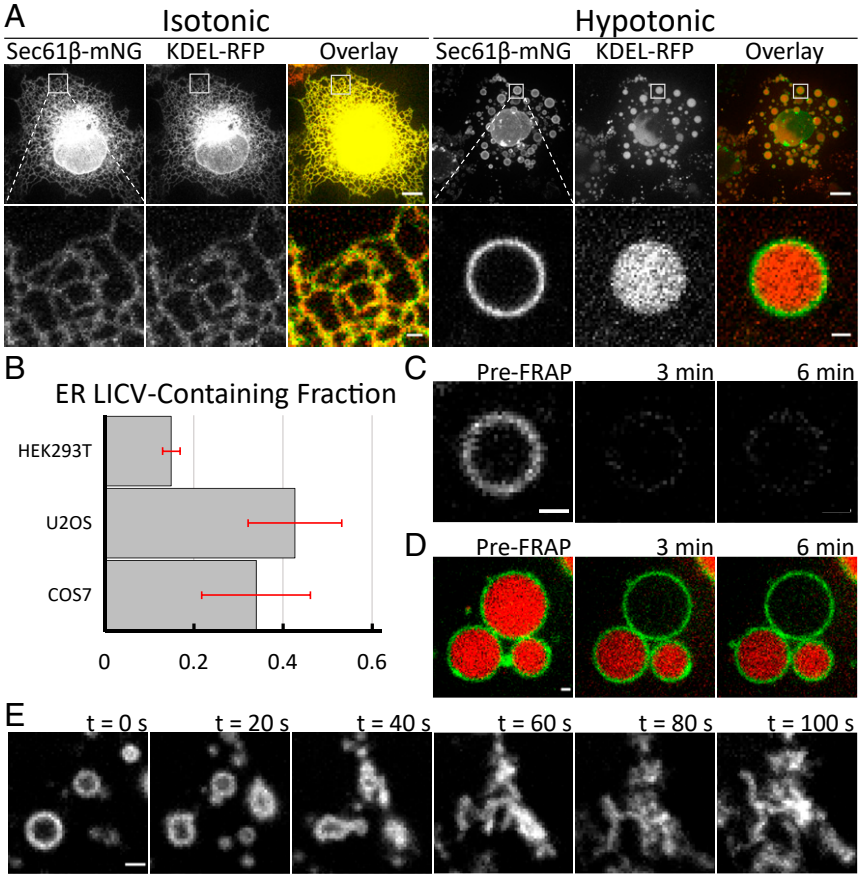

Fig. 1. Hypotonic treatment generates ER LICVs by vesiculation of the reticular ER network. (*A*) Columns 1 through 3 show a representative cell under isotonic conditions, cotransfected to visualize the ER membrane (green) and lumen (red) as indicated. Columns 4 through 6 show a representative cell under hypotonic conditions. The second row is a scaled image of the region indicated by the square. (*B*) The fractions of COS7, U2OS, and HEK293T cells containing ER LICVs following 10 min of hypotonic treatment. Error bars are the SDs from three independent experiments. (*C*) ER LICV membrane fluorescence does not recover after photobleaching the entire vesicle. Sec61b-mNG fluorescence is shown before photobleaching and at 3-min intervals afterward. (*D*) ER LICV lumen fluorescence does not recover after photobleaching the entire vesicle. The ER LICV membrane and lumen are labeled with Sec61β-mNG (green) and KDEL-RFP (red), respectively. Image sets for *C* and *D* are shown with identical brightness and contrast settings and can be compared directly. (*E*) ER LICVs retubulate and form an ER network within 2 min after cells are shifted to isotonic media. (Scale bars, 10 μm [*A*, *Top*] and 1 μm [*A*, *Bottom* and *C*–*E*].)

separation (8, 15, 36). Thus, we investigated whether, like GPMVs, ER LICVs show temperature-dependent phase separation into visible lipid domains. Two proteins with expected opposite lipid phase preferences were coexpressed in COS7 cells. One protein was Sec61β-mCherry, an ER-resident membrane protein with a short 21-amino-acid transmembrane domain, which is expected to partition into a disordered lipid phase. The other protein was an ER-retained glycosylphosphatidylinositol (GPI) anchored protein: Streptavidin binding protein-mNeonGreen-GPI (GPI-SBP-mNG). GPI-SBP-mNG is retained in the ER via the interaction of its N-terminal SBP domain with a streptavidin core targeted to the ER lumen with a C-terminal KDEL peptide (37). GPI-SBP-mNG is expected to preferentially partition into an ordered lipid phase due to the strong preference of GPI anchors for ordered lipid phase membranes (7, 8, 37).

At physiological temperature, Sec61β-mCherry and GPI-SBP-mNG were homogenously distributed in ER membranes both under isotonic and hypotonic (swelling) conditions (Fig. 2*A*, Isotonic and Hypotonic). Cells showed positive spatial correlation (quantified by Pearson correlation coefficient, ρ) between the two fluorescence channels under both these conditions ($\rho_{isotonic} = 0.91$ and $\rho_{hypotonic} = 0.65$) (Fig. 2*A*, *Top*). Fluorescence intensity profiles (linear profile across ER network in isotonic media, or radial profile around an ER LICV) confirmed the positive correlation between the two signals (Fig. 2*A*, *Bottom*).

We next cooled the hypotonically swollen cells to test if they underwent temperature-dependent phase separation. At room temperature and lower, ER LICV membranes demixed, with GPI-SBP-mNG and Sec61β-mCherry segregating into separate domains (Fig. 2*B*). We quantified the fraction of COS7 cells displaying microscopically visible domain formation on ER LICVs (Fig. 2*C*). We found a strong temperature dependency, with 50% of maximum demixing occurring at ∼20 °C. We then used a membrane order-sensitive probe, push-pull pyrene (PA) dye, to measure the relative lipid ordering of the two demixed domains in cooled ER LICV membranes (Fig. 2*D*) (38). PA dye undergoes a spectral shift to shorter wavelengths in ordered membranes. The order parameter, ϕ, defined as ratio of PA dye fluorescence intensities in GFP (C1) and RFP (C2) channels ($\phi = Int_{C2}/Int_{C1}$), gives an estimate of membrane order, with higher values of ϕ indicating more membrane disorder. We found that domains depleted of Sec61β on the demixed ER LICV surface showed increased lipid ordering (i.e., lower values of ϕ) compared to surrounding ER LICV membrane (Fig. 2*D*). This indicates that temperature-dependent demixing of ER LICVs involves segregation into membrane phases of different lipid order. We defined the Sec61β-depleted, ordered phase as the ER_o lipid phase and the Sec61β-enriched disordered phase as an ER_d lipid phase. Notably, GPI-SBP-mNG was enriched in ER_o lipid domains, as indicated by its preferential partitioning into domains depleted of Sec61β (see Fig. 2*B*).

ER_o domains in ER LICV membranes disappeared upon warming cells to 40 °C and reformed when the cells were again cooled to 5 ± 1 °C (Fig. 2 *E* and *F* and *SI Appendix*, Fig. S1), indicating that phase separation was reversible. To study the time-dependent behavior of proteins associated with ER_o and ER_d domains in cooled ER LICVs, we employed fluorescence recovery after photobleaching (FRAP) (*SI Appendix*, Fig. S2). At a temperature of 5 ± 1 °C, both GPI-SBP-mNG and Sec61β-mCherry within ER_d domains of ER LICV membranes showed ∼70% recovery of fluorescence signal within 25 s after photobleaching. By contrast, GPI-SBP-mNG within ER_o domains showed no recovery at this temperature. Upon warming to 40 °C, which caused ER_d and ER_o domains to disappear, both GPI-SBP-mNG and Sec61β-mCherry in the remixed LICV membranes showed full recovery within 25 s. These results suggest that in cells chilled to 5 °C, the ER_d domains have liquid-like properties, while the ER_o domains are in a solid "gel-like" phase. Whether ER_o domains retain their solid phase or become more liquid-like at higher temperatures (e.g., 20 °C) remains to be determined.

Hypotonic Treatment Generates Large Intracellular Vesicles from Other Organelles. We next examined the effects of hypotonic treatment on endosomes, lysosomes, mitochondria, peroxisomes, and LDs (Fig. 3). Endosomal membranes were labeled with enhanced green fluorescent protein (EGFP) attached to two tandem FYVE domains of the early endosome autoantigen 1 (EEA1) protein (2FYVE-EGFP). FYVE binds to phosphatidylinositol 3-phosphate (PI3P), a phospholipid enriched in early endosome membranes (39). To label endosomal luminal contents, cells were pulsed for 1 h with Alexa Fluor-594 conjugated dextran (10-kDa molecular weight) (40). Prior to hypotonic treatment, endosomes were composed mainly of small vesicles containing endocytosed dextran (Fig. 3, Endosomes, isotonic). After hypotonic treatment, these structures formed LICVs, which retained the luminal contents (Fig. 3, Endosomes, Hypotonic). Small spherical structures excluding the dextran label were sometimes visible inside the endosome LICVs (see arrowhead). These are likely luminal vesicles within the endosomal LICV.

To visualize the effect of hypotonic treatment on lysosomes, cells were transiently transfected with the lysosome-associated membrane glycoprotein (LAMP1)-YFP (yellow fluorescent protein) and treated with a 3-h pulse chase of fluorescent dextran (40). Before treatment, lysosomes were composed of small vesicles and tubular networks in cells (Fig. 3, Lysosomes, Isotonic). After hypotonic treatment, lysosomes formed micrometer-sized LICVs with LAMP1-positive membranes surrounding a lumen filled with dextran (Fig. 3, Lysosomes, Hypotonic). Some of the lysosomal LICVs had LAMP-positive vesicles inside of them, indicating they were possibly multivesicular bodies (*SI Appendix*, Fig. S3).

Mitochondria were examined in cells colabeled with a mitochondrial outer membrane protein, TOM20-YFP, and a mitochondrial matrix marker, mTagRFP-mito (41). Hypotonic treatment reshaped the tubular network of mitochondria (Fig. 3, Mitochondria, isotonic) into numerous mitochondrial LICVs (Fig. 3, Mitochondria, Hypotonic). In these vesicles, the matrix filled the space enclosed by the outer mitochondria membrane. It is known that the inner mitochondrial membrane is highly folded with cristae and can have a higher surface area than the outer membrane (30). Consistent with this, we sometimes found herniated mitochondrial LICVs in cells, in which the inner membrane and mitochondrial matrix extended into the cytosol from a large opening in the outer membrane (*SI Appendix*, Fig. S4).

Peroxisomes were labeled with peroxisome-associated membrane protein 2 (PXMP2) fused to mEmerald (31) and a peroxisomal luminal marker (SKL-mCherry) (42). Following hypotonic treatment, peroxisomes did not form LICVs and remained as diffraction-limited spots within cells (Fig. 3, Peroxisomes). Similarly, LDs labeled with adipose differentiation-related protein (ADRP) fused to GFP (43, 44) and BODIPY 665/676 did not form LICVs after hypotonic treatment (Fig. 3, LDs). Hypotonic treatment does not appreciably affect LD structure, likely because the hydrophobic lipid core of the LD creates a phase-separated volume that excludes water.

LICVs could be detected in hypotonically treated cells using label-free, spatial light interference microscopy (SLIM) without expressing any fluorescently tagged organelle markers (*SI Appendix*, Fig. S5). Many LICVs were immobile within the cells, while other LICVs appeared to undergo random, thermal motion (Movie S2). These results show that LICV formation occurs independently of the introduction of organelle-specific fluorescent tags.

ER LICVs Maintain Stable Interorganelle Contacts. Recent studies indicate that the ER establishes numerous contacts with other organelles of the cell (16–18, 27). These contact sites are difficult

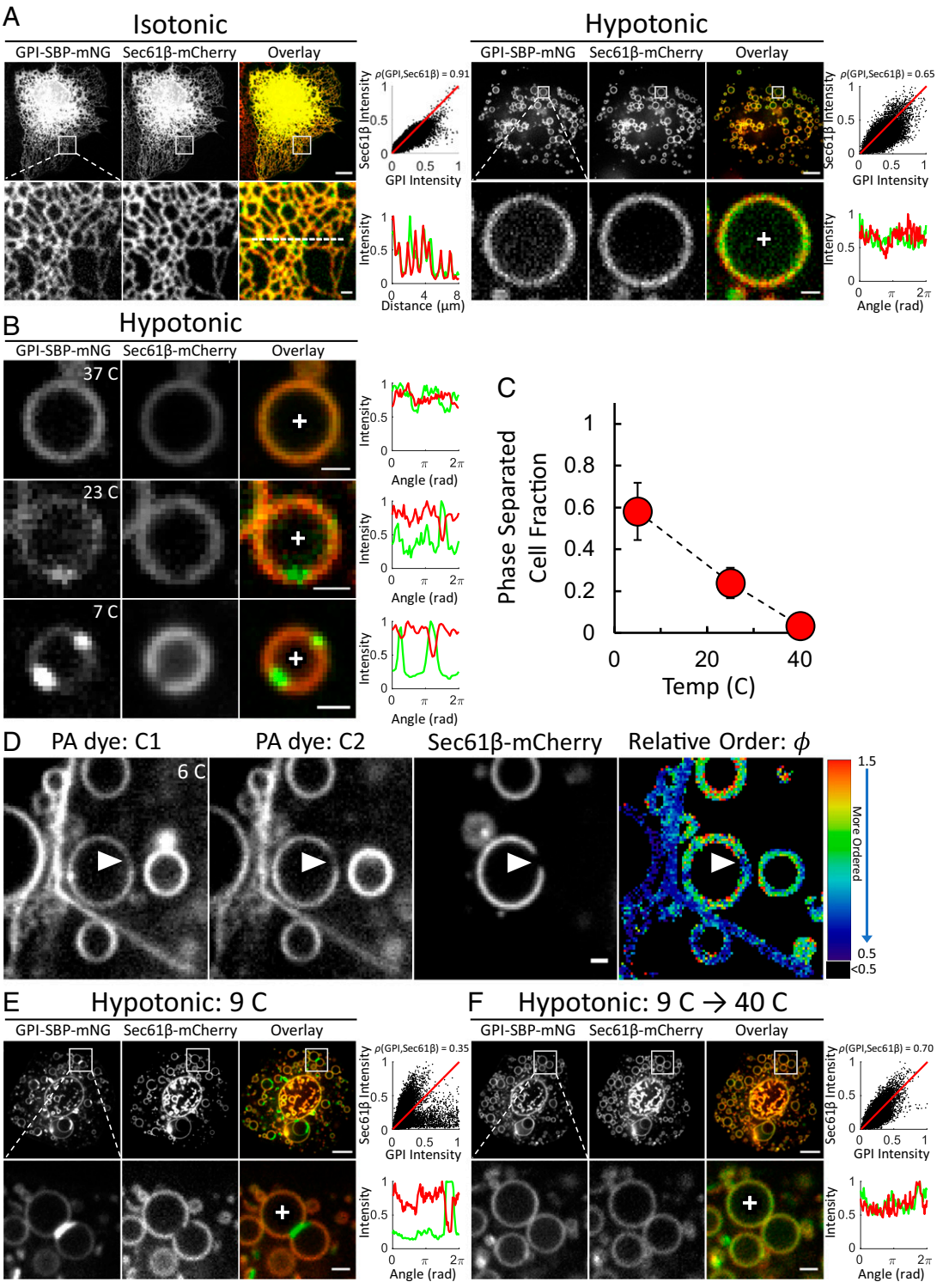

Fig. 2. ER LICVs exhibit reversible, temperature-dependent phase separation. (*A*, *Top*) GPI-SBP-mNG and Sec61β-mCherry colocalize on ER membrane in cells under isotonic and hypotonic conditions. GPI intensity versus Sec61β intensity is plotted along with the line $y = x$. (*A*, *Bottom*) A scaled image of the region indicated in the top row. The line profile intensity across the ER in the cells is plotted (*Left*), along with the radial intensity profile around the ER LICV in the swollen cell (*Right*). (*B*) Cells exhibit temperature dependent, micrometer-scale demixing of ER LICVs. Different cells were imaged at the temperature indicated. (*C*) Temperature dependence of the fraction of COS7 cells containing phase-separated ER LICVs. Error was estimated as the square root of the number of domain-containing cells and propagated to the cell fraction. $N_{5\ C} = 18/31$, $N_{25\ C} = 11/46$, $N_{40\ C} = 1/29$. (*D*) Ratiometric imaging of PA dye in phase-separated ER LICVs (6 ± 1 °C) shows a lower relative order parameter, $\phi = Int_{C2}/Int_{C1}$, at regions excluding Sec61β-mCherry (arrowhead). Nonmembrane-associated pixels are shown in black. (*E*, *Top*) A COS7 cell under hypotonic conditions with demixed ER membrane at 9 ± 1 C. (*E*, *Bottom*) A scaled image of the region indicated. (*F*) The same cell and the scaled region shown in *E* after warming to 40 ± 1 °C. GPI-SBP-mNG and Sec61β-mCherry remix in the ER LICV membrane. GPI intensity versus Sec61β intensity and the line $y = x$ (red) are plotted. The radial intensity profile around the ER LICV is also plotted for the scaled regions. Radial intensities plot the intensity beginning at the positive x axis (white cross), moving counterclockwise around the LICV. (Scale bars, 10 μm [*A*, *E*, and *F*, *Top*] and 1 μm [*A*, *B*, *D*, *E*, and *F*, *Bottom*].)

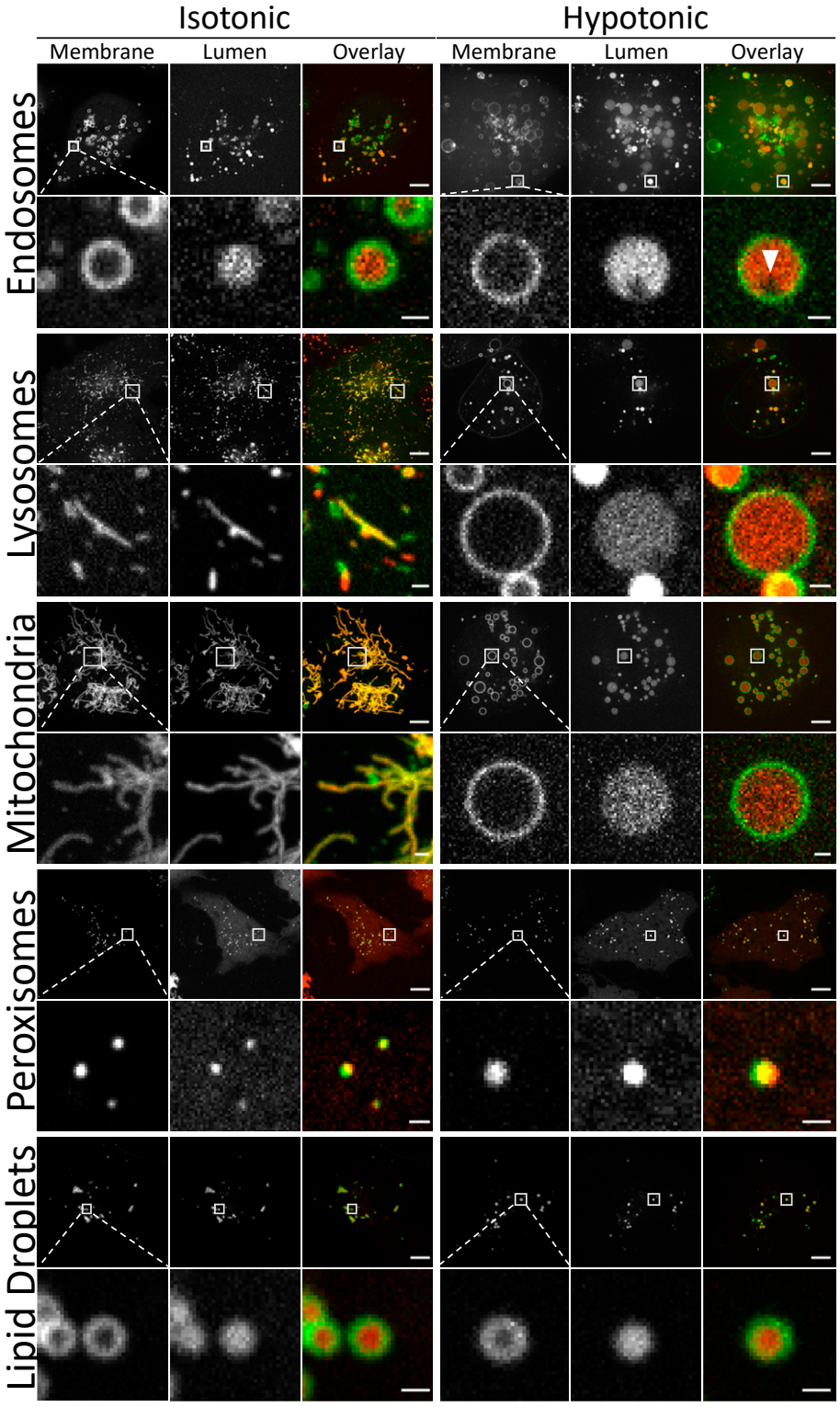

Fig. 3. The effect of hypotonic treatment on the internal organelles of COS7 cells. (*Left*) A representative cell under isotonic conditions cotransfected to visualize the the incidated organelle membrane and the luminal contents. (*Right*) A representative cell with the same organelle markers under hypotonic conditions. Under each full-cell image is a scaled imaged of the region indicated with the square. Endosomal membrane and lumen with are labeled with 2FYVE-GFP and 10-kDa dextran-Alexa Fluor 594. Lysosomal membrane and lumen are labeled with LAMP1-YFP and 10-kDa dextran-Alexa Fluor 594. Mitochondrial outer membrane and matrix are labeled with TOM20-YFP and mTagRFP-mito. Peroxisomal membrane and lumen are labeled with PXMP2-mEmerald and SKL-mCherry. LD phospholipid monolayer and neutral lipid core are labeled with ADRP-GFP and BODIPY 665/676. (Scale bars, 10 μm for full images and 1 μm for scaled regions.)

to study in live cells due to the complex, diffraction-limited, and time-varying nature of interorganelle contact sites. Thus, we investigated whether interorganelle contacts between LICVs were still present in cells after LICV generation (Fig. 4). We first examined whether ER contact sites with the PM persist after hypotonic treatment (Fig. 4, PM). These contact sites are important for Ca^{2+} and lipid exchange between these organelles (26). Cells were colabeled with the ER marker Sec61β-mCherry and the PM marker GPI-EGFP (45). After LICV generation, many ER LICVs were found stably associated with the PM (Fig. 4, PM, Hypotonic). In this cell, 39% out of 270 ER LICVs were associated with the PM.

Contact sites between the ER and endosomes were next examined. These contacts are known to coordinate endosomal fission and serve as important hubs for transfer of cholesterol to and from late endosomes (25, 27, 46). Cells were cotransfected with 2FYVE-EGFP to label endosomes and Sec61β-mCherry to label ER. After hypotonic treatment, many endosomal LICVs were found stably tethered to ER LICVs (Fig. 4, Endosomes). Ninety percent of the 68 endosomal LICVs within this cell were found to be associated with ER LICVs. A clear concentration of the 2FYVE construct at the endosome–ER LICV contact sites was also observed (see arrowhead pointing to punctum 2FYVE-GFP), implying that PI3P is enriched at the endosomal–ER contact sites. Consistent with this, prior work has shown that protrudin, an ER-localized protein with a PI3P-sensing FYVE domain, is concentrated at ER–late endosome contact sites (47). Conversely, we found that Rab5b-EGFP, another endosomal marker, was not concentrated at ER–endosome LICV contact sites (*SI Appendix*, Fig. S6) (48).

ER–lysosome contacts are important sites for regulated transfer of Ca^{2+} from the ER to lysosomes (49). To examine whether these contact sites persist after hypotonic treatment, cells were cotransfected with LAMP1-YFP to visualize lysosomes and Sec61β-mCherry to label ER. After hypotonic treatment, lysosomal LICVs were also found associated with ER LICVs in cells (Fig. 4, Lysosomes). In this cell, 22% of the 590 lysosomal vesicles were associated with ER LICVs.

ER–mitochondrion contacts mediate lipid and Ca^{+2} transfer between the ER and mitochondria (30, 50). To see if stable ER–mitochondrial LICV contacts persisted in hypotonically treated cells, cells were cotransfected with TOM20-YFP to label mitochondria and Sec61β-mCherry to label ER. After hypotonic treatment, many stable contacts between ER LICVs and mitochondrial LICVs were found (Fig. 4, Mitochondria). Of the 626 mitochondrial LICVs in this field of view, 96% were associated with ER LICVs.

The ER also forms contact sites with peroxisomes and LDs (27, 51). ER–peroxisome contact sites are thought to be involved in the metabolism of long-chain fatty acids and ER–LD contacts are sites of transfer of fatty acids and phospholipids (28, 52). Cells were cotransfected with Sec61β-mCherry to label ER and PXMP2-mEmerald to label peroxisomal membranes. After LICV media treatment, many ER LICVs existed in cells with peroxisomes decorating their surfaces (Fig. 4, Peroxisomes). In this cell, 93% of 267 peroxisomes were associated with ER vesicles. BODIPY 493/503 was then used to label the hydrophobic core of LDs in cells transfected with Sec61β-mCherry to label the ER. After hypotonic treatment, numerous LDs were also found on the surface of ER LICVs (Fig. 4, LDs). Fifty-six percent of the 206 LDs in this cell were associated with ER vesicles.

Together, these results suggest that ER LICVs maintain contacts with other major organelles in hypotonically treated cells. As the sites of contact between organelles were clearly observable because of their enlarged volumes and static nature, we could begin asking questions about protein organization at interorganelle contact sites.

Tethers Are Concentrated at Interorganelle Contacts. Tethers are proteins that serve to bridge opposing membranes of organelles to distances typically less than 40 nm, enabling interorganelle communication and molecular transfer (18). Since interorganellar contact sites are maintained as LICV contacts in cells following hypotonic treatment, we investigated the organization of protein tethers at the LICV contact sites.

The interactions between the ER–resident protein, vesicle-associated membrane protein-associated protein-B (VAPB), and the outer-mitochondrial membrane protein, protein tyrosine phosphatase-interacting protein 51 (PTPIP51), form an important type of ER–mitochondrial tether with a potential role in regulating autophagy (21, 53). Cells were transfected with VAPB-mEmerald and PTPIP51-mCherry and their distributions in ER and mitochondrial LICVs examined (Fig. 5*A*). Notably, the ER LICV showed reverse curvature at the ER–mitochondrial contact site due to tight tethering between the membranes. We performed a fluorescence loss in photobleaching (FLIP) experiment to reduce the VAPB and PTPIP51 signal in the LICV membrane away from the contact site as this would allow VAPB bound to PTPIP51 at contact sites to become visible (54). After the FLIP protocol, enhanced VAPB and PTPIP51 signal could be seen at the contact site, consistent with their role as ER–mitochondrial tethers (Fig. 5*A*, bar plot).

Mitofusin 1 (Mfn1) and mitofusin 2 (Mfn2) are extensively studied tethering proteins due to their key roles in mitochondria and ER organizations. Biochemical experiments have revealed that Mfn1 tethers membranes from two mitochondria units and drives fusion, whereas Mfn2 mediates ER–mitochondrial interaction and mitochondrial division (23, 29). To explore the organization of these proteins at LICV contact sites, LICVs were generated from cells expressing Mfn1-EGFP or Mfn2-YFP together with markers for mitochondrial membrane (TOM20-mCherry) or ER membrane (Sec61β) (Fig. 5 *B–D*). Mfn1-EGFP on mitochondrial LICVs was enriched within punctate structures at intermitochondrial contact sites (Fig. 5*B*, white arrowhead) and was absent both in ER LICV membrane and at ER–mitochondria contacts (Fig. 5*B*, yellow arrowhead). By contrast, Mfn2-YFP was present on both ER and mitochondrial LICV membranes (Fig. 5 *C* and *D*) and was enriched at both intermitochondria (Fig. 5*C*, arrowhead) and ER–mitochondria (Fig. 5*D*, arrowhead) contact sites. Notably, while Mfn2 signal intensity was approximately twofold higher at the ER–mitochondria LICV contact site compared to surrounding LICV membrane, fluorescent signals from Sec61β and TOM20 (which have no tethering function) were evenly distributed throughout the ER or mitochondrial LICV surface (Fig. 5*D*, bar plot). Our findings of concentrated Mfnl and Mfn2 at inter-LICV contact sites support their molecular roles as intermitochondrial and ER–mitochondrial tethers, as previously proposed (23). Collectively, these results offer an independent confirmation of the known tethering properties of Mfn1, Mfn2, VAPB, and PTPIP51 in cells.

Phase Behavior in ER LICVs Occurs at Interorganelle Contact Sites. Finally, we investigated the relationship between the ER–organelle contact sites and the locations of ER_o and ER_d domains found on ER LICVs. Cells were triply transfected with organelle markers, the ER_d marker Sec61β, and the ER_o marker GPI-SBP-mNG, treated with LICV media, and cooled to induce phase separation on the ER membranes. We then assessed ER_o/ER_d domain formation on ER LICVs at the locations of contacts with other organelles (Fig. 6).

We began by looking at ER contacts with PM (Fig. 6*A*, PM). We found that the ER–PM contact site coincides with ER_o domain formation on phase-separated ER LICV membranes. Similarly, ER–endosome and ER–mitochondrion contact sites were locations of ER_o domain formation on ER LICVs (Fig. 6*A*, Endosomes, Mitochondria). In contrast, ER–lysosome contacts occurred at ER_d lipid domains on ER LICVs (Fig. 6*A*, Lysosomes). Next, we examined the non-LICV-forming organelles: peroxisomes

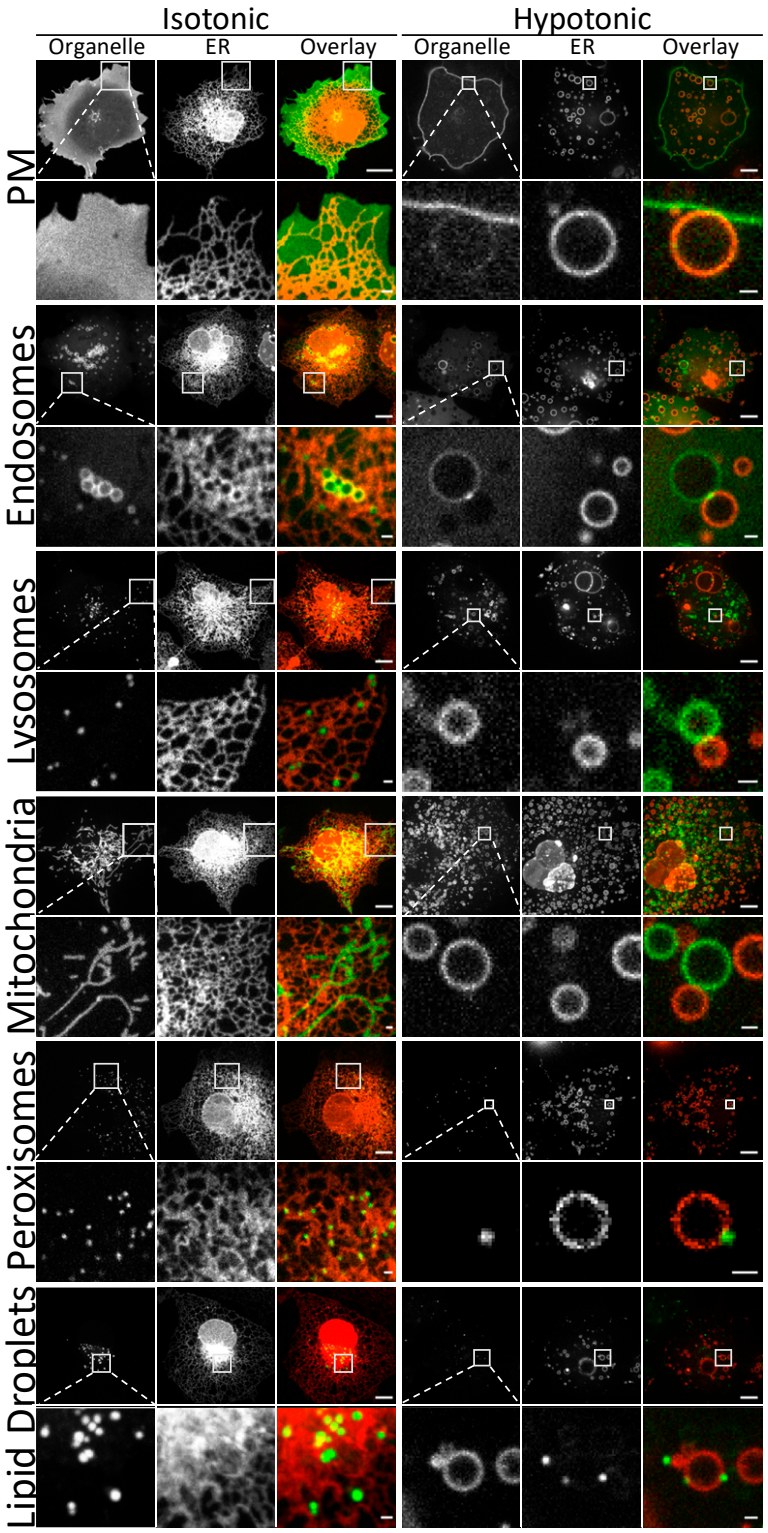

Fig. 4. Organelle–ER contact sites are ambiguous under isotonic conditions, while organelle contacts with ER LICVs are clear. Columns 1 through 3 show a representative cell under isotonic conditions that has been cotransfected to visualize the ER along with the indicated organelles within the cell. Columns 4 through 6 show a representative cell with the same labels under hypotonic conditions. Scaled images of the regions indicated with a square are shown in the bottom row for each organelle. The PM is labeled with GPI-GFP. Endosomes are labeled with 2FYVE-GFP. Lysosomes are labeled with LAMP1-YFP. Mitochondria are labeled with TOM20-YFP. Peroxisomes are labeled with PXMP2-mEmerald. LDs are labeled with BODIPY 493/503. The organelle labels of columns 1 and 4 are shown in green in the overlays and the ER is shown in the second and fifth columns, labeled with Sec61β-mCherry (red). (Scale bars, 10 μm for the full images and 1 μm for the scaled images.)

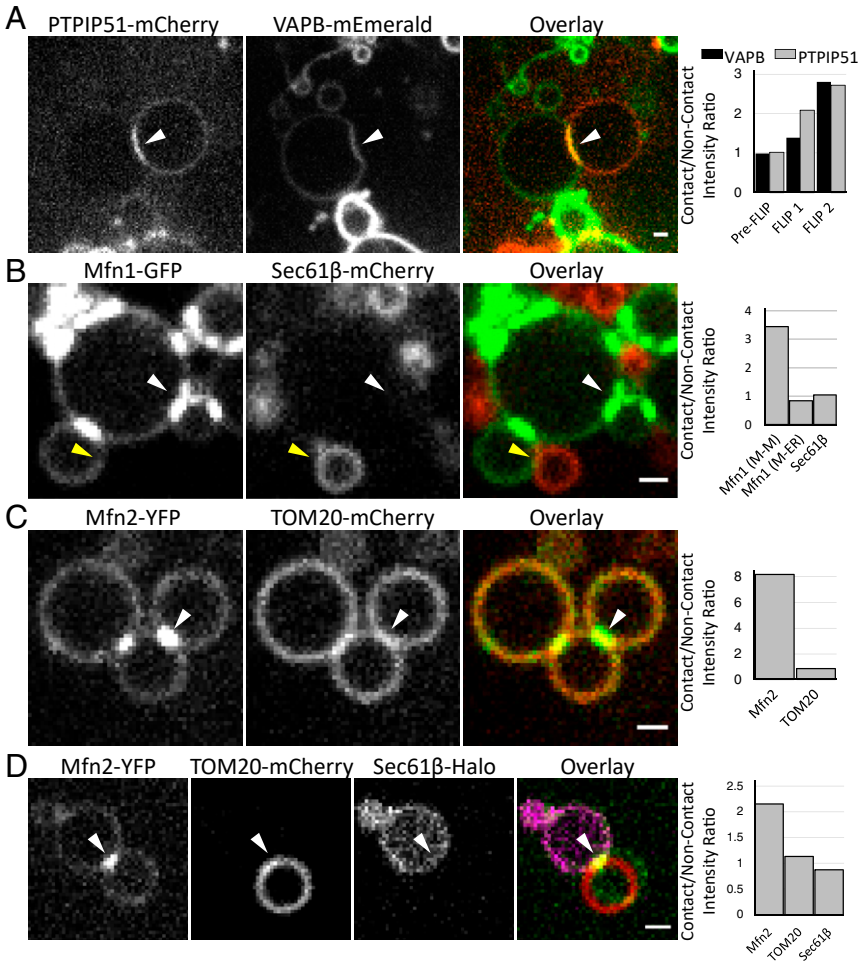

Fig. 5. Tethers are concentrated at LICV contacts. (*A*) PTPIP51 and VAPB concentration at ER–mitochondrial LICV contact sites (white arrow) is visible after two FLIP photobleaching protocols of membrane fluorescence. The bar plot shows the intensity ratio of the contact site fluorescence with the noncontact fluorescence before and after FLIP photobleaching protocols. (*B*) Puncta of Mfn1 form at intermitochondrial contact sites (white arrowhead). The bar plot shows Mfn1fluorescence enhancement at the intermitochondrial contact site, but Sec61β and Mfn1 are not enhanced at the ER–mitochoncrial LICV contact site, as expected (yellow arrowhead). (*C*) Puncta of Mfn2 form at intermitochondrial LICV contact sites (white arrowhead). The bar plot shows increased Mfn2 fluorescence intensity at the inter-LICV mitochondrial contact site. TOM20 is not concentrated at the contact site but appears brighter because of fluorescence on two membranes. (*D*) Puncta of Mfn2 form at ER–mitochondrial LICV contact sites (white arrowhead). The bar plot shows increased Mfn2 intensity at the ER–mitochondrial LICV contact site, while TOM20 and Sec61β are not concentrated at the contact. In *B–D*, when fluorescence is present on both contacting membranes, the ratio represents the contact site fluorescence intensity divided by the sum of fluorescence intensity on both membranes at noncontact regions. The images above are representative from multiple experiments. (Scale bars, 1 μm for *A–D*.)

and LDs. Peroxisomes localized to ER_d lipid domains and were frequently located at the interfaces between ER_o and ER_d domains. (Fig. 6*A*, Peroxisomes). In contrast, LDs were associated with ER_o domains on phase-separated ER LICV membranes (Fig. 6*A*, LDs).

Based on the above results, there appeared to be a pattern in the preference for ER_o- or ER_d- domain localization within ER–organelle LICV contact sites. The PM, endosomes, mitochondria, and LDs are organelles with lipid transfer functions with the ER. These organelles contacted ER_o domains on phase-separated ER LICVS. Lysosomes receive their lipid components from endosomes and were associated with ER_d domains. Peroxisomes, which receive lipid components from multiple organelles, were associated with the ER_d/ER_o domains interfaces on phase-separated ER LICVs.

Since peroxisomes receive membrane components from both the ER and mitochondria, we investigated the possibility that peroxisomes associated with the ER_d/ER_o interface are associated with mitochondria as well as the ER. We used three-color fluorescence microscopy to examine the localizations of ER, mitochondria, and peroxisomes in chilled, hypotonically treated cells. The radial intensity profile around the ER LICV showed that a peroxisome (arrow) is located at the ER_d/ER_o interface on the ER LICV surface (Fig. 6*B*). A mitochondrion is also bound at the ER_o domain of this ER LICV (i.e., the TOM20 peak is at the position of the Sec61β fluorescence signal minimum). Thus, we find that peroxisomes can be associated with ER_o domains through a tri-junction arrangement involving a mitochondrion. Collectively, these results suggest that organelles with lipid transport functions to and from the ER are associated with ER_o domains on phase-separated ER LICVs.

Discussion

Hypotonicity has been used to study cellular mechanisms of volume regulation as well as for creating spherically shaped blebs of PM to study protein–protein interactions (55, 56). However, relatively little attention has been paid to the internal membranes of the cell under hypotonic conditions. Here, we show that hypotonic treatment generates LICVs derived from different organelles (including ER, endosomes, lysosomes, and mitochondria) and that the LICVs can be used to characterize

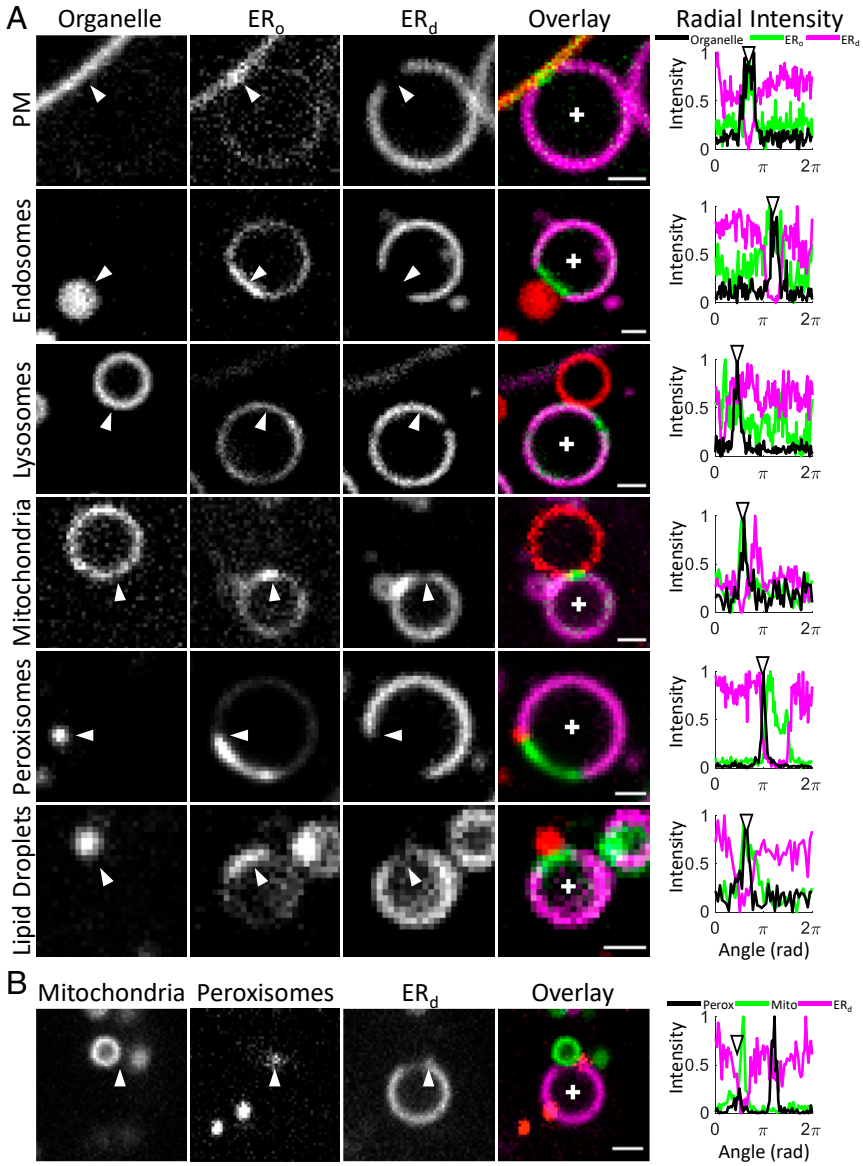

Fig. 6. ER LICVs demonstrate phase behavior at interorganelle contact sites (white arrows). (*A*) ER–organelle LICV pairs in cells that have been chilled to induce ER membrane phase separation. The PM is labeled with GPI-mCherry. Endosomes are labeled with 10-kDa dextran-Alexa Fluor 594. Lysosomes are labeled with LAMP1-mCherry. Mitochondria are labeled with TOM20-mCherry. Peroxisomes are labeled with SKL-mCherry. LDs are labeled with BODIPY 665/676. The ER_o and ER_D domains of phase-separated ER LICVs are labeled with GPI-SPB-mNG and Sec61β-JF646, respectively. For LDs, the ER is labeled with Sec61β-mCherry. The organelle, ER_o, and ER_d membranes in the overlays are colored in red, green, and magenta, respectively. The radial intensity profile plots the fluorescence intensity in a counterclockwise direction around the ER LICV beginning at the *x* axis (white cross). ER_o, ER_d, and organelle fluorescence intensity are plotted in green, magenta, and black, respectively. (*B*) Peroxisomes (white arrow) associate with ER_o domains at ER–mitochondrial contact sites. The radial intensity profile plots the fluorescence intensity in a counterclockwise circle around the ER LICV. The images above are representative from multiple experiments. (Scale bars, 1 μm for *A* and *B*.)

various membrane properties and contact site organization of these organelles.

The spherical shape of LICVs makes them amenable to a wide range of existing biophysical techniques used to study the properties of lipids and proteins in the PM. For example, the LICV provides an ideal surface for membrane protein diffusion measurements, decoupled from the effects of the time-varying, diffraction-limited, and complex topologies of organelles in the active cell. Another possible experimental application is the use of optical tweezer-based pulling experiments in order to measure the strength of inter-LICV tethering. Upon a return to isotonic conditions, cells rapidly tubulate and fuse independent ER LICVs into a connected ER network. Thus, ER LICV generation could also provide a means to study ER membrane tubulation and fusion by enabling an initial state of the ER that is devoid of a diffraction-limited, complex topology. Currently, shaping and tubulation effects by proteins have only been studied in vitro with purified organelles (57), with cell-derived GPMVs, or with synthetic giant unilamellar vesicles (33–35, 58).

After hypotonic treatment, ER LICVs maintained stable interorganelle contacts. Some of these contacts could have been formed or released during LICV generation, while others could simply be vesicles resting next to each other within the confined volume of the cell. However, many contacts among LICVs likely represent bona fide sites of interorganelle tethering, existent within the cell at the time of LICV generation. Supporting this, we

found concentrations of four different tethering proteins (VAPB, PTPIP51, Mfn1, and Mfn2) at ER–mitochondrial contacts. Prior work studying organelle contact sites has shown that they persist after harsh mechanical or chemical separation methods (59). Indeed, ER–mitochondrial contacts are strong enough to survive cell lysis and centrifugation—the original method enabling biochemical studies of these contacts (59, 60). Thus, it is likely that contact sites persist in cells through LICV generation and that the observed concentration of protein tethers at these contact sites is physiologically relevant to the living cell.

We showed that ER LICVs can be phase-separated into microscopically observable ER_o and ER_d domains in a temperature-dependent fashion. The process of domain formation was reversible, indicating that the phase behavior was not an effect of salt or pH changes within the cytosol. ER_o domain formation occurred at organelle contacts with the PM, endosomes, and mitochondria. Interestingly, lysosomes and peroxisomes were tethered to ER_d domains on the phase-separated ER membrane, while peroxisomes could be associated with ER_o domains through an additional interaction with a mitochondrion. Why ER organelle contact sites show this specific arrangement remains to be explored, but the results imply there is both lipid- and protein-based specificity associated with the contact sites.

The lipid characteristics of ER_o and ER_d domains in ER LICVs still remain to be explored. Toward this end, we found that fluorescence from GPI and Sec61β proteins in ER_d domains recovered after photobleaching, while GPI in ER_o domains showed no recovery at 5 °C. This suggests ER_o domains represent a solid or gel-like phase. Cholesterol is an active regulator of membrane fluidity. It can disrupt the tight packing of saturated lipid acyl chains at low temperatures (when they are likely to be in solid/gel phase), fluidizing the membrane and driving it to an L_o-like phase. Because ER membrane has a substantially lower amount of cholesterol than the PM, one possibility is that the low amount of cholesterol in the ER membrane is insufficient to fluidize ER_o domains formed at 5 °C. Consequently, the ER_o domains acquire a solid or gel-like phase at low temperatures.

GPMVs and other in vitro membrane models have been crucial for understanding physical properties and sorting mechanisms of PM components. Except for the recent discoveries of microscale phase-partitioned domains in yeast vacuole membranes (61), no similar tool exists to assess membrane properties and functions of intracellular organelles. Thus, this work demonstrates that LICVs provide a valuable tool to study a wide variety of biophysical phenomena on the internal membranes of eukaryotic cells.

Methods

Cell Culture and Organelle Labeling. Cells, cultured in Dulbecco's modified Eagle's medium (DMEM) containing 10% fetal bovine serum and supplemented with L-glutamine, were seeded in Matrigel-coated 35-mm glass-bottom Petri dishes (MatTek). Twenty-four hours after seeding, at ∼70% confluency level, cells were transiently transfected using Lipofectamine 3000 and 200 to 800 ng of the plasmids indicated, according to the manufacturer's instructions. Cells were imaged 12 to 24 h after transfection. COS7 cells were used in all experiments unless otherwise indicated.

For the loaded endosome experiments, cells were seeded and transfected as above with the 2FYVE-GFP construct. Just prior to imaging, a 1-h pulse with 0.5 mM dextran (10-kDa dextran conjugated to Alexa Fluor 594, D22913; Thermo Fisher), followed by extensive rinses with phosphate-buffered saline (PBS) buffer was performed. Cells were then treated with hypotonic media and imaged. For the dextran-loaded lysosome experiments, cells were pulsed for 3 h with 0.5 mM dextran, followed by extensive rinses with PBS buffer, and a chase of 3 h in full media. Cells were then swelled and imaged.

Hypotonic Cell Treatment. Cells were treated with hypotonic LICV media (5% DMEM in water, pH ∼ 7), incubated at 37 °C with 5% CO_2 for 10 min to allow for ER-LICV generation, and then imaged. We find that hypotonically treated COS7 cells returned to isotonic media undergo apoptosis and die, probably due to the presence of herniated mitochondria. This occurs after the ER has retubulated to form an interconnected network. Hypotonically treated cells are stable in the dish for over an hour. After longer exposure to hypotonic media, cells detach from the dish and presumably die. Detached cells were not imaged or utilized in this study.

Cell Microscopy. Live-cell confocal imaging was performed using a customized Nikon TiE inverted microscope with a Yokogawa spinning-disk scan head (CSU-X1; Yokogawa) and an Andor iXon electron-multiplying charge-coupled device (EMCCD) camera. Fluorescence was collected through standard filters using a 100× Plan-Apochromat 1.40 numerical aperture oil objective (Nikon). Cells were imaged incubated with a Tokai Hit stage-top incubator at 37 °C and 25 °C under 5% CO_2. Chilled cells were imaged under atmospheric CO_2. Sample temperature was monitored and maintained with a QE-1HC Heated/Cooled Quick Exchange Platform controlled by a CL-100 Single Channel Bipolar Temperature Controller from Warner Instruments.

For the PA dye experiments, cells transiently transfected with Sec61β-mCherry were treated with 1:20 DMEM containing 200 nM PA dye. After incubation at 37 °C for 10 min, cells were chilled to induce visible phase separation in the mCherry signal, and PA dye signal was imaged with 405-nm laser diode excitation. Data were acquired sequentially in two scans with 400-ms exposure time for both on the GFP and RFP (red fluorescent protein) channels on the Nikon described above. During acquisition, the Andor iXon EMCCD camera gain was set to 1. A region containing no membrane was averaged to determine the background contribution in each channel's data. The background was subtracted and the intensity ratio of the RFP to the GFP channel pixel values was calculated.

SLIM was performed with a Phi Optics SLIM unit attached to a Zeiss inverted microscope with a Plan-Neofluar 63×/1.3 Imm Corr Ph3 M27 water immersion objective with a Hammamatsu C11440 digital camera. Cells were imaged at 37 °C with 5% CO_2 using a Tokai Hit stage-top incubator.

Data Analysis. Line scans and radial intensity profiles were created using the line-scan function in Fiji. LICVs and cells were counted manually with the built-in cell counter plugin (62, 63).

Pearson correlation coefficients between GPI-SBP-mNG and Sec61β-mCherry fluorescence images were calculated with MATLAB according to the equation $\rho(A, B) = \frac{1}{N-1}\sum_{i=1}^{N}\left(\frac{A_i-\mu_A}{\sigma_A}\right)\left(\frac{B_i-\mu_B}{\sigma_B}\right)$. μ_A and μ_B are means of vectors A and B; σ_A and σ_B are the SDs of A and B. Cell images were segmented to remove background pixels prior to calculation of correlation coefficients.

To measure the fractions of U2OS, COS7, and HEK293T cells displaying LICVs, large stitched images were acquired at 40× magnification and 37 °C. The 5 × 5 stitched fields of view at a single z-height were imaged in three separate dishes of cells singly transfected with Sec61β-mNeonGreen. The total number of cells in the image was counted and cells were counted as containing LICVs if they had at least one visible LICV within them. The fraction for each dish was calculated and an SD was calculated from these fractions.

To measure the temperature dependence of ER LICV domain formation, cells were imaged after incubation for 30 min at the temperature described. Cells containing stably located LICVs found and inspected for micrometer-scale domain formation with depression of Sec61β and enhancement of the GPI-SBP constructs. A representative image was then acquired. Images were later inspected for the presence of visible domains with FIJI and cells were counted. The fraction of cells with domains was calculated from these counts.

FRAP measurements were performed at the temperature indicated. GPI-SBP-mNG was photobleached with a 488-nm laser at 100% power for 1 s. Sec61β-mCherry and KDEL-mCherry were photobleached in the same manner with a 561-nm laser. Data were acquired for 5 s prior to the photobleaching laser pulse and for up to 25 s afterward. The recovery data plotted have been generated by first subtracting the time-dependent background contribution from the FRAP region data. A second region was chosen which was not photobleached, and after subtraction of the same background contribution the ratio of these regions was calculated. This data were then normalized from zero to one, with one equal to the mean of the first 20 s of time data for the pre-FRAP ratio. The simple FRAP model was fit with MATLAB.

The FLIP experiment was performed by repeated photobleaching of ER and mitochondrial LICV membranes in regions away from sites where these two organelles made contact.

All numerical analyses and figure plots were done with MATLAB.

Data Availability. All data supporting the findings of the study are included in the paper.

ACKNOWLEDGMENTS. We thank Dr. Ilya Levental and Dr. William Prinz for helpful discussions; Drs. Luke Lavis, Yacheng Liao, Heejun Choi, Chris Obara, and Chi-Lun Chang for reagents and experimental advice; and Dr. Andrey S. Klymchenko (University of Strasbourg, France) for supplying the PA dye.

1. S. J. Singer, G. L. Nicolson, The fluid mosaic model of the structure of cell membranes. *Science* **175**, 720–731 (1972).
2. K. Simons, E. Ikonen, Functional rafts in cell membranes. *Nature* **387**, 569–572 (1997).
3. A. Toulmay, W. A. Prinz, Direct imaging reveals stable, micrometer-scale lipid domains that segregate proteins in live cells. *J. Cell Biol.* **202**, 35–44 (2013).
4. P. Sengupta *et al*., A lipid-based partitioning mechanism for selective incorporation of proteins into membranes of HIV particles. *Nat. Cell Biol.* **21**, 452–461 (2019).
5. M. Belkin, W. G. Hardy, Relation between water permeability and integrity of sulfhydryl groups in malignant and normal cells. *J. Biophys. Biochem. Cytol.* **9**, 733–745 (1961).
6. R. E. Scott, R. G. Perkins, M. A. Zschunke, B. J. Hoerl, P. B. Maercklein, Plasma membrane vesiculation in 3T3 and SV3T3 cells. I. Morphological and biochemical characterization. *J. Cell Sci.* **35**, 229–243 (1979).
7. T. Baumgart *et al*., Large-scale fluid/fluid phase separation of proteins and lipids in giant plasma membrane vesicles. *Proc. Natl. Acad. Sci. U.S.A.* **104**, 3165–3170 (2007).
8. K. R. Levental, I. Levental, "Chapter two - Giant plasma membrane vesicles: Models for understanding membrane organization" in *Current Topics in Membranes*, A. K. Kenworthy, L. Domains, Eds. (Academic Press, 2015), vol. 75, pp. 25–57.
9. I. Levental, F. J. Byfield, P. Chowdhury, F. Gai, T. Baumgart, P. A. Janmey, Cholesterol-dependent phase separation in cell-derived giant plasma-membrane vesicles. *Biochem. J.* **424**, 163–167 (2009).
10. S. L. Veatch, S. L. Keller, Separation of liquid phases in giant vesicles of ternary mixtures of phospholipids and cholesterol. *Biophys. J.* **85**, 3074–3083 (2003).
11. E. Sezgin, I. Levental, S. Mayor, C. Eggeling, The mystery of membrane organization: Composition, regulation and roles of lipid rafts. *Nat. Rev. Mol. Cell Biol.* **18**, 361–374 (2017).
12. I. Levental, D. Lingwood, M. Grzybek, U. Coskun, K. Simons, Palmitoylation regulates raft affinity for the majority of integral raft proteins. *Proc. Natl. Acad. Sci. U.S.A.* **107**, 22050–22054 (2010).
13. H. J. Sharpe, T. J. Stevens, S. Munro, A comprehensive comparison of transmembrane domains reveals organelle-specific properties. *Cell* **142**, 158–169 (2010).
14. J. C. Rayner, H. R. Pelham, Transmembrane domain-dependent sorting of proteins to the ER and plasma membrane in yeast. *EMBO J.* **16**, 1832–1841 (1997).
15. J. Lippincott-Schwartz, R. D. Phair, Lipids and cholesterol as regulators of traffic in the endomembrane system. *Annu. Rev. Biophys.* **39**, 559–578 (2010).
16. S. Cohen, A. M. Valm, J. Lippincott-Schwartz, Interacting organelles. *Curr. Opin. Cell Biol.* **53**, 84–91 (2018).
17. A. M. Valm *et al*., Applying systems-level spectral imaging and analysis to reveal the organelle interactome. *Nature* **546**, 162–167 (2017).
18. M. Eisenberg-Bord, N. Shai, M. Schuldiner, M. Bohnert, A tether is a tether is a tether: Tethering at membrane contact sites. *Dev. Cell* **39**, 395–409 (2016).
19. T. Burgoyne, S. Patel, E. R. Eden, Calcium signaling at ER membrane contact sites. *Biochim. Biophys. Acta* **1853**, 2012–2017 (2015).
20. E. R. Eden *et al*., Annexin A1 tethers membrane contact sites that mediate ER to endosome cholesterol transport. *Dev. Cell* **37**, 473–483 (2016).
21. P. Gomez-Suaga *et al*., The ER-mitochondria tethering complex VAPB-PTPIP51 regulates autophagy. *Curr. Biol.* **27**, 371–385 (2017).
22. N. Shai, M. Schuldiner, E. Zalckvar, No peroxisome is an island - Peroxisome contact sites. *Biochim. Biophys. Acta* **1863**, 1061–1069 (2016).
23. O. M. de Brito, L. Scorrano, Mitofusin 2 tethers endoplasmic reticulum to mitochondria. *Nature* **456**, 605–610 (2008).
24. T. Klecker, S. Böckler, B. Westermann, Making connections: Interorganelle contacts orchestrate mitochondrial behavior. *Trends Cell Biol.* **24**, 537–545 (2014).
25. A. A. Rowland, P. J. Chitwood, M. J. Phillips, G. K. Voeltz, ER contact sites define the position and timing of endosome fission. *Cell* **159**, 1027–1041 (2014).
26. C. J. Stefan, Building ER-PM contacts: Keeping calm and ready on alarm. *Curr. Opin. Cell Biol.* **53**, 1–8 (2018).
27. M. J. Phillips, G. K. Voeltz, Structure and function of ER membrane contact sites with other organelles. *Nat. Rev. Mol. Cell Biol.* **17**, 69–82 (2016).
28. M. Schuldiner, M. Bohnert, A different kind of love - lipid droplet contact sites. *Biochim. Biophys. Acta Mol. Cell Biol. Lipids* **1862**, 1188–1196 (2017).
29. G. Chandhok, M. Lazarou, B. Neumann, Structure, function, and regulation of mitofusin-2 in health and disease. *Biol. Rev. Camb. Philos. Soc.* **93**, 933–949 (2018).
30. T. Pollard *et al*., "Endoplasmic Reticulum" in *Cell Biology* (Saunders Elsevier, 2nd Edition, 2008), p. 345.
31. S. Munro, H. R. B. Pelham, A C-terminal signal prevents secretion of luminal ER proteins. *Cell* **48**, 899–907 (1987).
32. J. Nixon-Abell *et al*., Increased spatiotemporal resolution reveals highly dynamic dense tubular matrices in the peripheral ER. *Science* **354**, aaf3928 (2016).
33. R. Dasgupta, M. S. Miettinen, N. Fricke, R. Lipowsky, R. Dimova, The glycolipid GM1 reshapes asymmetric biomembranes and giant vesicles by curvature generation. *Proc. Natl. Acad. Sci. U.S.A.* **115**, 5756–5761 (2018).
34. Y. F. Barooji, A. Rørvig-Lund, S. Semsey, S. N. S. Reihani, P. M. Bendix, Dynamics of membrane nanotubes coated with I-BAR. *Sci. Rep.* **6**, 30054 (2016).
35. K. E. Ward, J. P. Ropa, E. Adu-Gyamfi, R. V. Stahelin, C2 domain membrane penetration by group IVA cytosolic phospholipase A_2 induces membrane curvature changes. *J. Lipid Res.* **53**, 2656–2666 (2012).
36. G. van Meer, D. R. Voelker, G. W. Feigenson, Membrane lipids: Where they are and how they behave. *Nat. Rev. Mol. Cell Biol.* **9**, 112–124 (2008).
37. G. Boncompain *et al*., Synchronization of secretory protein traffic in populations of cells. *Nat. Methods* **9**, 493–498 (2012).
38. Y. Niko, P. Didier, Y. Mely, G. Konishi, A. S. Klymchenko, Bright and photostable push-pull pyrene dye visualizes lipid order variation between plasma and intracellular membranes. *Sci. Rep.* **6**, 18870 (2016).
39. C. C. Scott, P. Cuellar-Mata, T. Matsuo, H. W. Davidson, S. Grinstein, Role of 3-phosphoinositides in the maturation of Salmonella-containing vacuoles within host cells. *J. Biol. Chem.* **277**, 12770–12776 (2002).
40. I. Martinez *et al*., Synaptotagmin VII regulates Ca(2+)-dependent exocytosis of lysosomes in fibroblasts. *J. Cell Biol.* **148**, 1141–1149 (2000).
41. R. N. Day, M. W. Davidson, The fluorescent protein palette: Tools for cellular imaging. *Chem. Soc. Rev.* **38**, 2887–2921 (2009).
42. S. J. Gould, G. A. Keller, N. Hosken, J. Wilkinson, S. Subramani, A conserved tripeptide sorts proteins to peroxisomes. *J. Cell Biol.* **108**, 1657–1664 (1989).
43. V. T. Salo *et al*., Seipin regulates ER-lipid droplet contacts and cargo delivery. *EMBO J.* **35**, 2699–2716 (2016).
44. D. L. Brasaemle *et al*., Adipose differentiation-related protein is an ubiquitously expressed lipid storage droplet- associated protein. *J. Lipid Res.* **38**, 2249–2263 (1997).
45. J. M. Rhee, M. K. Pirity, C. S. Lackan, J. Z. Long, G. Kondoh, J. Takeda, A.-K. Hadjantonakis, In vivo imaging and differential localization of lipid-modified GFP-variant fusions in embryonic stem cells and mice. *Genesis* **44**, 202–218 (2006).
46. L. P. Wilhelm *et al*., STARD3 mediates endoplasmic reticulum-to-endosome cholesterol transport at membrane contact sites. *EMBO J.* **36**, 1412–1433 (2017).
47. C. Raiborg *et al*., Repeated ER-endosome contacts promote endosome translocation and neurite outgrowth. *Nature* **520**, 234–238 (2015).
48. M. Chiariello, C. B. Bruni, C. Bucci, The small GTPases Rab5a, Rab5b and Rab5c are differentially phosphorylated in vitro. *FEBS Lett.* **453**, 20–24 (1999).
49. A. G. Garrity *et al*., The endoplasmic reticulum, not the pH gradient, drives calcium refilling of lysosomes. *eLife* **5**, e15887 (2016).
50. A. A. Rowland, G. K. Voeltz, Endoplasmic reticulum-mitochondria contacts: Function of the junction. *Nat. Rev. Mol. Cell Biol.* **13**, 607–625 (2012).
51. S. Raychaudhuri, W. A. Prinz, Nonvesicular phospholipid transfer between peroxisomes and the endoplasmic reticulum. *Proc. Natl. Acad. Sci. U.S.A.* **105**, 15785–15790 (2008).
52. J. L. Costello, I. G. Castro, T. A. Schrader, M. Islinger, M. Schrader, Peroxisomal ACBD4 interacts with VAPB and promotes ER-peroxisome associations. *Cell Cycle* **16**, 1039–1045 (2017).
53. R. Stoica *et al*., ER-mitochondria associations are regulated by the VAPB-PTPIP51 interaction and are disrupted by ALS/FTD-associated TDP-43. *Nat. Commun.* **5**, 3996 (2014).
54. J. Lippincott-Schwartz, E. Snapp, A. Kenworthy, Studying protein dynamics in living cells. *Nat. Rev. Mol. Cell Biol.* **2**, 444–456 (2001).
55. F. Lang *et al*., Functional significance of cell volume regulatory mechanisms. *Physiol. Rev.* **78**, 247–306 (1998).
56. C. King, M. Stoneman, V. Raicu, K. Hristova, Fully quantified spectral imaging reveals in vivo membrane protein interactions. *Integr. Biol.* **8**, 216–229 (2016).
57. N. Wang, T. A. Rapoport, Reconstituting the reticular ER network - Mechanistic implications and open questions. *J. Cell Sci.* **132**, jcs227611 (2019).
58. M. Simunovic, G. A. Voth, A. Callan-Jones, P. Bassereau, When physics takes over: BAR proteins and membrane curvature. *Trends Cell Biol.* **25**, 780–792 (2015).
59. J. E. Vance, Phospholipid synthesis in a membrane fraction associated with mitochondria. *J. Biol. Chem.* **265**, 7248–7256 (1990).
60. C. D. Williamson, D. S. Wong, P. Bozidis, A. Zhang, A. M. Colberg-Poley, Isolation of endoplasmic reticulum, mitochondria, and mitochondria-associated membrane and detergent resistant membrane fractions from transfected cells and from human cytomegalovirus-infected primary fibroblasts. *Curr. Protoc. Cell Biol.* **68**, 3.27.1–3.27.33 (2015).
61. A. Y. Seo *et al*., AMPK and vacuole-associated Atg14p orchestrate μ-lipophagy for energy production and long-term survival under glucose starvation. *eLife* **6**, e21690 (2017).
62. J. Schindelin *et al*., Fiji: An open-source platform for biological-image analysis. *Nat. Methods* **9**, 676–682 (2012).
63. C. A. Schneider, W. S. Rasband, K. W. Eliceiri, NIH image to ImageJ: 25 years of image analysis. *Nat. Methods* **9**, 671–675 (2012).